

T DOCUMENTATION PAGE

1a. RE 1			1b. RESTRICTIVE MARKINGS NA		
2a. SE 1			3. DISTRIBUTION/AVAILABILITY OF REPORT Distribution Unlimited; Approved for Public Release		
2b. DECLASSIFICATION/DOWNGRADING SCHEDULE NA			5. MONITORING ORGANIZATION REPORT NUMBER(S) NA		
4. PERFORMING ORGANIZATION REPORT NUMBER(S) INDU/DC/GMH/TR-88-36			7a. NAME OF MONITORING ORGANIZATION ONR		
6a. NAME OF PERFORMING ORGANIZATION Indiana University		6b. OFFICE SYMBOL (If applicable) NA	7b. ADDRESS (City, State, and ZIP Code) 800 N. Quincy Street Arlington, VA 22217		
6c. ADDRESS (City, State, and ZIP Code) Department of Chemistry Bloomington, IN 47405		9. PROCUREMENT INSTRUMENT IDENTIFICATION NUMBER Contract N00014-86-K-0366			
8a. NAME OF FUNDING/SPONSORING ORGANIZATION		8b. OFFICE SYMBOL (If applicable)	10. SOURCE OF FUNDING NUMBERS		
8c. ADDRESS (City, State, and ZIP Code)		PROGRAM ELEMENT NO.	PROJECT NO.	TASK NO. R&T Code 4134006	WORK UNIT ACCESSION NO.
11. TITLE (Include Security Classification) Tomographic Image Reconstruction Techniques for Spectroscopic Sources: Theory and Computer Simulations					
12. PERSONAL AUTHOR(S) C. A. Monnig, K. A. Marshall, G. D. Rayson, and G. M. Hieftje					
13a. TYPE OF REPORT Technical		13b. TIME COVERED FROM TO	14. DATE OF REPORT (Year, Month, Day) 11 July 1988		15. PAGE COUNT 32
16. SUPPLEMENTARY NOTATION Accepted for publication in Spectrochim. Acta, Part B					
17. COSATI CODES			18. SUBJECT TERMS (Continue on reverse if necessary and identify by block number)		
FIELD	GROUP	SUB-GROUP	Tomography, Plasma, ICP, Multielement Analysis, Mapping, Inductively coupled plasma, Auger		
1					
19. ABSTRACT (Continue on reverse if necessary and identify by block number) Computerized tomography (CT) offers one method for accurately reconstructing the spatial features of a spectroscopic source having arbitrary geometry. With computer-simulated lateral projections as the input data, the potential advantages and problems associated with several CT algorithms were compared. In general, CT offers greater spatial information content than more commonly used image-reconstruction techniques, but at the added expense of more involved post-processing calculations and more elaborate experimental instrumentation.					
20. DISTRIBUTION/AVAILABILITY OF ABSTRACT <input checked="" type="checkbox"/> UNCLASSIFIED/UNLIMITED <input type="checkbox"/> SAME AS RPT <input type="checkbox"/> DTIC USERS			21. ABSTRACT SECURITY CLASSIFICATION Distribution Unlimited E		
22a. NAME OF RESPONSIBLE INDIVIDUAL Gary M. Hieftje			22b. TELEPHONE (Include Area Code) (812) 335-2189		22c. OFFICE SYMBOL -

4

DTIC
ELECTE
AUG 16 1988
S D

OFFICE OF NAVAL RESEARCH

Contract N14-86-K-0366

R&T Code 4134006

TECHNICAL REPORT NO. 36

TOMOGRAPHIC IMAGE RECONSTRUCTION TECHNIQUES FOR
SPECTROSCOPIC SOURCES: THEORY AND COMPUTER SIMULATIONS

by

C. A. Monnig, K. A. Marshall, G. D. Rayson, and G. M. Hieftje



Prepared for Publication
in
SPECTROCHIMICA ACTA, PART B

Indiana University
Department of Chemistry
Bloomington, Indiana 47405

11 July 1988

Accession For	
NTIS GRA&I	<input checked="checked" type="checkbox"/>
DTIC TAB	<input type="checkbox"/>
Unannounced	<input type="checkbox"/>
Justification	
By	
Distribution/	
Availability Codes	
Dist	Avail and/or Special
A-1	

Reproduction in whole or in part is permitted for
any purpose of the United States Government

This document has been approved for public release
and sale; its distribution is unlimited

1. Introduction

Diagnostic studies are essential to the understanding of atomization, ionization, and excitation processes that occur in spectroscopic sources (e.g., flames, plasmas, etc.). In the course of such studies, it is often necessary to resolve spatially the processes being investigated. In the past, these studies almost exclusively have utilized lateral-projection data collected from a single viewing direction. These data are the integrated signals produced by the object along the viewing direction and therefore require post-processing to produce the true three-dimensional spatial structure of the source under study.

For the special case where the source can be shown to be optically thin and to have a well defined geometry and position, an area inversion matrix can be calculated and used to convert the lateral projection data into their spatially resolved equivalents [1]. Here, we will focus on the most commonly encountered situation where the source is known to possess circular or elliptical symmetry. Under these circumstances, the inverse Abel transform can be applied to the lateral projection data to obtain the spatially (radially) resolved information [1-4].

Although the inverse Abel transform (the "Abel inversion") is perhaps best known for its applications in astrophysics, analytical spectroscopists have also applied it to atom reservoirs in atomic spectroscopy [1,5-7]. One analytically significant spectroscopic source which has been widely investigated via inverse Abel-transformed data is the inductively coupled plasma (ICP). The radially resolved information made available by this technique allows the events in the plasma to be probed in a non-invasive manner and can be used to determine atomization and excitation conditions within the ICP under typical analysis conditions.

Despite the obvious utility of the inverse Abel transform, it suffers from several significant limitations including an intolerance to noise in the input data, and the requirement for a known geometry in the object under investigation.* In practice, an observed lateral profile will always contain some noise. The sensitivity of the inverse Abel transform to this noise often necessitates the use of elaborate smoothing and filtering techniques before the data can be inverted [5-7]. Furthermore, lateral-projection data are often not symmetric, even when the object under investigation is thought to be so

* For the examples presented in this paper, when the inverse Abel transform is discussed, the transform for circularly symmetric data will be assumed. When the elliptically symmetric transform is used, an *a priori* knowledge of the eccentricity of the ellipse is required for the area inversion matrix to be calculated. Consequently, this is a less commonly encountered application of this transform. However, many of the same arguments for the circularly symmetric transform can be extended to the elliptically symmetric transform.

[5,8]. In this case, the choice of the center point about which the data will be transformed becomes critically important. Small changes in the selected center of symmetry can result in significant differences in the transformed data. More important, the existence of an asymmetric projection violates the basic assumption of circular symmetry which is required for the rigorous use of the inverse Abel transform. Thus, no matter which point in the asymmetric data set is selected as the center, a "true" reconstruction of the original object can never be obtained from this transform. Any additional structural information contained in the lateral projection is lost by transforming the data in a way which forces circular symmetry. Nevertheless, researchers continue to apply this transform to lateral projection data which are obviously asymmetric. Several attempts have been made to modify the Abel-inversion process to accept asymmetric data and to return meaningful radially resolved data [9,10]. However, the resulting spatial maps are, at best, useful only for gaining a qualitative understanding of spectroscopic sources.

Yet another problem with the inverse Abel transform is that it generates the greatest uncertainties in the reconstructed data for points in the central region of a calculated radial profile [4]. This limitation is particularly troublesome in the investigation of sources such as the ICP, where the region of greatest analytical interest is in the center of the discharge.

Fortunately, many of the foregoing problems can be overcome by reconstructing an image with a more general computed-tomography (CT) algorithm. In a strict sense, the inverse Abel transform is a form of CT. However, for the purposes of this paper we will consider CT to include only those techniques which assume no special symmetry in the object under investigation. Since CT requires no preliminary assumption of symmetry, the problem of selecting the symmetry point is eliminated. Moreover, the impact of random noise on the acquired data is much less severe in the reconstructed image with most CT approaches than with the inverse Abel transform. As a result, information about the center of the object can be more reliable.

In the studies presented here, mathematical models (phantoms) which describe an object to be studied and projections from those phantoms were calculated. Reconstructed images based on these projections were then computed utilizing several popular CT algorithms. These results reveal that many of the problems which plague the use of the inverse Abel transform can be overcome. In particular, the CT reconstruction algorithms that are explored exhibit superior freedom from the effects of noise in the input data. Additionally, if suitable care is taken while data are collected, the information content of the reconstructed image can be markedly improved.

2. THEORY

Image reconstruction from projections is a problem which has its history in the early roots of the modern physical sciences. The primary goal in image reconstruction is to determine the distribution in space of the species which give rise to, or perturb a signal of interest. Although initial attempts to address specific parts of this problem can be traced to the nineteenth century, JOHANN RADON's classic 1917 paper [11] is generally considered to provide the first practical solution to the general problem and to lay the foundation for what has developed into the modern field of computed tomography. Briefly, RADON posed the following problem. If the lateral projections of an object of arbitrary shape are known for all projection angles ϕ , can an accurate picture of this object be constructed from only this information? His solution to this problem was to develop a line-integral formula (now known as the Radon transform) to perform the necessary mathematical operation. If projections from all angles are known, this formula can be used to estimate from the projections the true spatial features of the object under investigation. Unfortunately, under practical analysis conditions, projections cannot be collected at all possible angles. Therefore, a number of algorithms have been developed which are based on the Radon transform but which allow an estimate of the object under investigation to be calculated from a discrete number of projections. Since the successful introduction of these algorithms, CT has found widespread application in the physical and biological sciences, with particular emphasis being placed, in recent years, on the use of CT for medical imaging.

To understand the ramifications of computed tomography, we must consider two transform spaces: feature space and Radon space. Feature space is the Euclidian space described by traditional geometric principles. In feature space would be found the real, point-by-point spatial features of an object. For the purpose of the following discussion we shall consider feature space to have two dimensions, although the arguments presented here can easily be generalized to any number of dimensions (n). Radon space is where the Radon transform of feature space exists. Untreated projection data collected in the laboratory would lie in Radon space. Radon space can also have any number of dimensions, although the two-dimensional case will again be used here for simplicity.

When lateral-projection data are collected, they are the Radon-space representation of the object under investigation. To reconstruct the image, one need only transform the data from Radon to feature space. Hence, it is the transform of these Radon-space data to feature space which is the operation used to reconstruct an image from its lateral

projections. The inverse Radon transform in a polar-coordinate system is shown in Eqn.

(1)

$$f(r, \theta) = \frac{1}{2\pi^2} \int_0^\pi \int_{-\infty}^\infty \frac{1}{q' - q} \frac{\partial l(q, \phi)}{\partial q} dq d\phi \quad (1)$$

where $q' = \sin(\theta - \phi)$, q is the position on the projection from the arbitrarily assigned central position (e.g., the position on the detector array), ϕ is the projection angle, and θ is the angle in the arbitrarily established coordinate system referenced to a point in the reconstruction currently under consideration. If the geometric limitation of circular symmetry is imposed upon the object, all projections are equivalent (e.g., independent of angle ϕ) and Radon's formula reduces to Abel's transform equation. Further discussion of the mathematical intricacies of the Radon transform can be found in the monograph by DEANS [12].

Unfortunately, there is no widely applicable and efficient algorithm to perform directly the inverse Radon transform; consequently, it is rarely used explicitly. Instead, other procedures are usually substituted. Several of the more popular reconstruction algorithms are described below. It will not be attempted here to describe the procedures in mathematical detail; instead, their range of applicability and utility will be assessed. The reader is directed elsewhere [13-20] for more detailed descriptions of the mathematics behind each of the reconstruction methods.

2.1. Backprojection

Backprojection [13-16], the simplest of the reconstruction methods, is illustrated schematically in Fig. 1. Consider a square, homogeneous object contained in some observation plane XY (the section of a homogeneous cube indicated on the top of Fig. 1). If lateral projections of the object are collected along the x and y axes, a crude reconstruction of the original object can be obtained by reversing the projection process (backprojection). This reverse operation is shown on the bottom of Fig. 1. In this method, each section of the ray which generates one point in the lateral projection is assumed to contribute equally to the signal. Conceptually, the process of backprojection can be thought of as smearing the lateral projection across an area of feature space where the reconstruction is to be formed. The reconstructed image is generated where the rays sum together. The density at each point in the reconstructed image can be estimated by the sum of all rays which pass through that point. As projections from additional angles are collected and backprojected, the reproduction more closely resembles the original object.

Repeating this exercise with an object of more complicated geometry reveals that the more complex the structure, the greater the number of projections which are needed to generate an accurate reconstruction. Consequently, in practice, a large number of projections are usually collected at different angles around the object.

The primary advantage of backprojection is its conceptual simplicity and ease of implementation. Unfortunately, backprojection does not reproduce the image as faithfully as do other reconstruction methods. Because the backprojected signal is averaged along its entire optical path, star-like artifacts are observed extending from the object of interest (the lightly shaded region in the bottom part of Fig. 1). These artifacts result in an overall blurring of the reconstructed image. However, if each lateral projection is convoluted with an appropriate filter function before it is backprojected, these star-like projections can be reduced or eliminated; in addition, noise can be reduced and desired features enhanced in the reconstructed image. This method, known as the filtered backprojection or convolution method [13-18] has been shown to enjoy considerable freedom from the effects of noise in the input data [18].

To illustrate the filtered backprojection approach, consider the example in Fig. 2. Figure 2A shows a lateral projection of calcium atomic emission (422.7 nm) obtained low in an ICP discharge. Figure 2B shows a selected frequency-domain convolution filter, in this case a Parzen filter multiplied by a ramp function (PARZN filter). Details concerning this and other suitable filters can be found elsewhere [17]. The convolution process is implemented by Fourier transforming the lateral-projection data, followed by a multiplication of the transformed values by the frequency-domain filter. The inverse Fourier transform of this product is the convoluted or "filtered" projection (Fig. 2C). The relative ease of implementation of the convolution method, its speed of execution, and the accuracy of the reconstructed image make this method the most popular for reconstruction of data obtained by the collection of parallel beams.

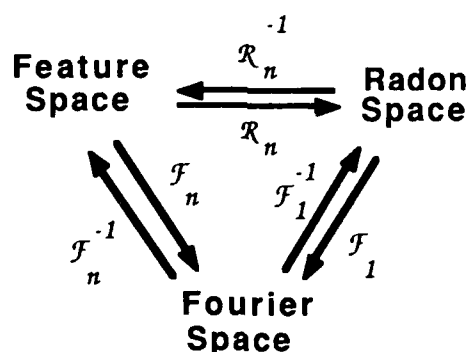
2.2. Rho-Filtered Layergram

As mentioned previously, the backprojection method produces a blurred estimate of the original object. The rho-filter layergram (RFL) reconstruction method attempts to alleviate this problem by post-processing of the data after the backprojection. With this technique, the image produced by backprojection is subjected to a two-dimensional Fourier transform. The resulting data are then multiplied by a suitable filter function and the product subjected to an inverse two-dimensional Fourier transform. As with the convolution method, choice of the appropriate filter function is critical for an accurate

reconstruction to be produced. Furthermore, aliasing of structures near the edge of the reconstruction region can be a problem [13,17].

2.3. Fourier Inversion

An alternative method for image reconstruction uses a path through Fourier space [13,15,19,20]. It can be shown [12] that the relationship among feature, Radon, and Fourier space is:



where \mathcal{R} refers to a Radon transform and \mathcal{F} refers to a Fourier transform. The subscript 1 indicates a one-dimensional transform whereas a subscript n pertains to an n -dimensional transform. The superscript -1 designates an inverse transform. Simply stated, a series of one-dimensional Fourier transforms of Radon space followed by an n -dimensional inverse Fourier transform is equivalent to an n -dimensional inverse Radon transform of Radon space. This connectivity allows the equivalent of Radon or inverse Radon transforms to be computed when the Fourier transforms are known or can be calculated. Practically, to reconstruct an axial slice from an emission source, each lateral projection is Fourier transformed and then mapped into polar raster space. These data are interpolated to map this polar coordinate information onto an x - y grid. Finally, an inverse two-dimensional Fourier transform is computed to generate the reconstructed image. This process is shown schematically in Fig. 3.

The availability of high-speed discrete Fourier-transform algorithms makes the path through Fourier space an attractive reconstruction approach. Unfortunately, the Fourier-reconstruction method is somewhat sensitive to noise in the original projection data. In addition, aliasing of structures near the edge of the reconstruction region can occur. Consequently, the convolution method is usually favored over the Fourier path. However, a recently introduced direct Fourier-inversion algorithm promises improved

fidelity in the reconstructed image while maintaining the advantage of reconstruction speed [21].

2.4. Iterative Reconstruction Techniques

A final class of techniques for image reconstruction, which will not be explored extensively in this paper, is known collectively as the iterative reconstruction methods [13-16]. These techniques estimate the image to be reconstructed, and modify the estimate iteratively so the predicted projections progressively resemble more closely the projections collected experimentally. An example of how this reconstruction might be carried out is shown in Fig. 4. The top array of numbers represents the original object being investigated. The empirically determined projection is indicated on the right side of this array and consists simply of the intensity sum along the respective projection axes. The reconstructed image is shown in the array at the bottom of Fig. 4. The top number in each array element represents the initial estimate of the "true" structure of the object. From this estimate, a projection is calculated along the same angle as the experimentally determined projection. The calculated projection is compared with the experimentally determined projection and a correction factor calculated. In this example, the integrated signal across the top row of the reconstruction estimate equals 11, while the empirically determined signal was 8. Each array element in the image estimate which contributed to that data point in the lateral projection is therefore multiplied by $8/11$ to obtain the "improved" estimate of the object's structure (the array numbers in parentheses). Once the correction has been accomplished for each ray in the projection, the new estimate of the structure is used to calculate a projection at a new angle. This process is repeated until the estimated structure generates lateral projections which closely match the experimentally determined projections.

The images reconstructed by the iterative reconstruction techniques are, in general, not much better than those determined by the reconstruction methods mentioned previously and often require much longer computational reconstruction times. However, the iterative reconstruction methods have achieved recent popularity because they allow images to be reconstructed from projections collected in unusual geometries which would not be applicable to the reconstruction methods described previously.

3. COMPUTER SIMULATIONS

Computer simulations were used to investigate the properties of, and to identify possible problems with several CT algorithms. A summary of these investigations follows. All simulations were generated on a VAX 11/780 computer (Digital Equipment, Maynard,

Massachusetts). Phantoms, projection data and tomographic reconstructions were calculated by the SNARK77 program [13]. Unless otherwise stated, absorption projection data were generated from the phantom at 125 separate projection angles with 99 detector positions at each angle. Likewise, images were reconstructed with a convolution algorithm utilizing a bandlimiting filter described elsewhere [13]. Symmetric inverse Abel transforms were implemented with a FORTRAN program based on an algorithm discussed by BLADES [10]. Contour plots of the output data (with 10 equally spaced contour levels) were generated with the DI-3000 graphics package (Precision Visuals, Boulder, Colorado) and displayed on a Talaris 800 laser printer (Talaris Systems Inc., San Diego, California).

3.1. Alternative Reconstruction Methods

Let us first assess the capabilities and limitations of alternative reconstruction algorithms. A representative and useful phantom, shown in Fig. 5A, contains regions of both high and low spatial frequency. The density step on the edge of the structure provides a high spatial frequency for the reconstruction. The constant density in the body of the phantom has a very low spatial frequency. A reconstruction of this object using the Fourier path is shown in Fig. 5B. The artificial structure within the body of the reconstructed object and uneven nature of its borders indicates the limitations of the Fourier method, particularly when compared with the RFL (Fig. 5C) and convolution (Fig. 5D) algorithms. The differences between the RFL and convolution reconstructions are relatively small, although the image produced by the convolution algorithm seems to be slightly more faithful in regions of the object where the intensity is uniform.

3.2. Aliasing

From Fig. 5, it is clear that reconstruction from projections often generates artifacts in the final image. These artifacts are the result of limitations in both the reconstruction algorithms and the detection system. A thorough understanding of how these artifacts can arise is critical to the minimization of their effect.

In practice, projections to be used for CT reconstructions must be collected at discrete angles around the object under investigation. The highest spatial frequency that can be reproduced in a CT image is determined by the separation of detectors in a single projection for the image. The Nyquist criterion predicts the relationship

$$d = \frac{1}{2v} \quad (2)$$

where d is the separation between adjacent detector elements or projection positions and v is the maximum spatial frequency that can be accurately represented. If measurements

are obtained at inter-detector separations greater than distance d , structures will be aliased and spurious low-frequency artifacts will appear in the reconstructed image. Analogous arguments can be applied to the number of angles at which projections must be measured. The minimum number of angles (m) should meet the following criterion for bandlimiting resolution [16]:

$$m = \frac{\pi}{2} n \quad (3)$$

where n is the number of data points in a single lateral projection. These m number of scans should be equally spaced over an angle of at least 180 degrees. Failure to meet this sampling criterion can result in aliasing of object structures. In contrast, if this latter sampling criterion is exceeded, the reconstructed image is overdetermined and noise in the final CT image is reduced. A more complete discussion of the effect of viewing geometry on the information content of the reconstructed image is presented by KLUG and CROWTHER [22].

The effect of angular aliasing is depicted in Fig. 6. Figure 6A shows the original phantom whereas Figs. 6B, 6C, and 6D represent the use of 5, 25, and 125 viewing angles, respectively, when applied to a convolution reconstruction algorithm with 99 lateral detector positions. As is readily apparent in Fig. 6B, severe aliasing of the object occurs when projections from only five angles are collected. As the number of projections increases to 25 and 125 (Figs. 6C and 6D, respectively), the reconstructed image approximates the original phantom much more closely. Clearly, the accuracy of the reconstruction is strongly influenced by the number of angles from which the source is viewed. Of course, the "star pattern" chosen for illustrative purposes here contains higher spatial frequencies than would be encountered in most spectroscopic sources; this fact should be considered throughout the following discussion.

The effect of aliasing caused by too few resolution elements in a lateral projection (e.g., not enough elements in a detector array) is revealed in Fig. 7. If only 11 detector readings are collected at each angular position, strong aliasing of the high-spatial-frequency structures is observed (Fig. 7B). The inability of the reconstruction algorithm to reproduce the sharp edges of the object is a clear indication of this aliasing. As the number of detector positions at each angle is increased (33 and 99 in Figs. 7C and 7D, respectively), these effects diminish until they become almost imperceptible. As in Fig. 6, the regions of the object which display sharp transitions (high spatial frequency) determine the viewing geometry which is required. Typical spectroscopic sources do not

usually display such sharp structural variations, so a smaller number of viewing positions might be adequate.

When spatial frequencies are aliased, another kind of artifact can appear at sharp boundaries in the image. This artifact, called the Gibbs phenomenon or ringing [16,23], appears as an overshoot of the density of the object under investigation near sharp boundaries. This phenomenon can be suppressed by filtering the spatial frequencies of the object so there is a "roll-off" of the higher spatial frequencies in place of a sharp cutoff. Not surprisingly, such filtering can also degrade the spatial resolution of the reconstructed image.

3.3. Other Artifacts

Another common source of artifacts observed in many CT images is variation in the sensitivity of the detectors when more than one detector is used to collect the projection data. This effect manifests itself as streaks and swirls in the reconstructed image. Fortunately, normalization of the detector response can reduce this effect to imperceptible levels.

A primary requirement for the reliable implementation of CT methods is that the object under investigation must be stable while all needed projections are collected. If the object changes or moves during the collection of the projection data, streak artifacts are introduced into the image. The only way to eliminate this effect is to reduce the period of time over which the data are collected.

All real data carry noise, and it is desirable for a reconstruction algorithm to be relatively immune to it. Often, CT reconstruction algorithms contain some type of smoothing or frequency-domain filtering as an integral part of the reconstruction; such reconstruction algorithms exhibit a significant tolerance for noise in the projection data. Furthermore, in CT no single reconstructed spatial data point is determined from a single projection. This feature gives rise to a type of signal averaging which reduces noise in the reconstructed image. One example of the capabilities of the convolution CT reconstruction algorithm to handle noise is shown in Fig. 8. In this example, random noise was added to each of the lateral projections used to reconstruct the images. Figure 8B shows the reconstruction obtained when no noise was added to the lateral projections. Figures 8C through 8F display the reconstructions as noise of increasing amplitude is introduced into the data. Importantly, reasonably accurate reconstruction is possible even when the standard deviation of the noise is equal to the signal value (Fig. 8E). Not until the standard deviation of the noise is ten times the signal amplitude do we observe a significant distortion in the reconstructed image (Fig. 8F). Of course, in this example, the added

noise was statistically random. Non-random noise could affect the image in a different manner. Nevertheless, CT is capable of accepting input data which would be difficult if not impossible for the inverse Abel transform to handle without extensive prefiltering.

3.4. Comparison of CT and Abel Inversion

To illustrate some of the advantages of computed tomography in situations where inverse Abel transforms have traditionally been applied, we have generated phantoms which simulate inductively coupled plasmas of differing geometries and have reconstructed their images using the convolution CT algorithm and the inverse Abel transform. The results of these simulations are shown in Figs. 9 through 12. In these examples, hypothetical projections were collected at 60 different angles with 101 elements in the detector array. In Figs. 9A and 9B, the three-dimensional and contour plots (feature-space representations) of a simulated circularly symmetrical ICP are presented, respectively. In Figs. 9C and 9D the corresponding reconstructed image obtained with the convolution CT algorithm is shown. In Figs. 9E and 9F the reconstructed images obtained when lateral projections at right angles to each other were generated by inverse Abel transformation. The contour plots of the radial data obtained from the inverse Abel transform are not shown, but they must, by definition, display circular symmetry. Not surprisingly, for a source which is known to be circularly symmetric, the inverse Abel transform is superior for reconstructing images both in terms of processing time and fidelity of the reconstructed image. The CT reconstruction exhibits a relatively high level of fluctuations in the reconstructed image when compared with the image produced by Abel inversion. This additional noise can perhaps be explained by the additional degrees of freedom which must be employed to handle objects of arbitrary geometry. Abel inversion would therefore be the reconstruction method of choice for sources of circular symmetry and low noise. For very noisy sources, extensive signal averaging and digital filtering of the projection would be needed to generate as faithful a reconstruction as provided by CT.

Figure 10 shows the results of a similar study in which an elliptically symmetrical phantom was employed. Predictably, the inverse Abel transform produces an image that is highly dependent upon which lateral projection is used as the input data set. For the two examples shown here, the lateral projections were collected along the major and minor axes of the ellipse (Figs. 10E and 10F, respectively). Understandably, the output data sets differ significantly, even though lateral projections from all positions around the phantom are symmetrical. If this situation were to occur in a real spectroscopic source and if an observer were to collect two orthogonal projections, both taken at angles bisecting the major and minor axes of the ellipse, the lateral data obtained would reduce to

identical radial properties when subjected to an Abel inversion transform. Obviously, this coincidence is unlikely, but no more so than the one we have shown to accentuate the differences. Nevertheless, the CT reconstruction reproduces the phantom with relative ease, the major difference again being spurious features in the reconstructed image.

In Fig. 11, the elliptically symmetrical phantom has its maximum skewed off center. Again, the CT reconstruction closely resembles the phantom, but the inverse Abel transform provides a reconstruction which differs significantly from the phantom. As is common, the center of "symmetry" used here for Abel inversion was chosen as the peak intensity. Selection of this center point is critical as previously discussed. If another criterion for center-point selection were used, the results would be quite different for the case shown in 11E which is the Abel inversion of an asymmetric lateral profile. Figure 11F represents the Abel inversion of the only symmetric lateral profile obtainable from this skewed elliptical source. The symmetry of this projection makes the selection of the center much less prone to error.

In the final example, shown in Fig. 12, the skewed elliptically symmetrical phantom of Fig. 11 has had a local discontinuity imposed upon it. As with the other examples, CT reproduces the object with satisfying fidelity. In contrast, the two images reconstructed by the inverse Abel transform provide misleading information about the object being investigated. From data collected at one angle (Fig. 12E), the Abel inversion implies that the phantom is extremely narrow and has a central maximum. The other Abel reconstruction (Fig. 12F) suggests that the source is very wide and has a central minimum. Clearly, neither reconstruction is close to the "true" structure. From these examples we must conclude that applying an inverse Abel transform to data which has even a small degree of asymmetry is risky and should cast doubt upon any quantitative interpretations based on those data.

4. CONCLUSIONS

These simulations have shown that computed tomography can be a powerful method for determining the spatial structure of spectroscopic sources of arbitrary geometry. No attempt has been made to investigate the properties of reconstruction algorithms for divergent beam geometry, although such methods exist [13]. The choice of the reconstruction algorithm should be dictated by the required fidelity of the reconstructed image, the computational speed required, geometry of the structures under investigation, and physical limitations imposed by the instrument which collects the projection data.

Although CT offers a significant improvement over image-reconstruction methods currently in use by analytical chemists, it does not solve all of the problems which might

be encountered. A primary assumption behind the tomographic reconstruction algorithms is that the object being investigated is optically thin. Other, extraordinary measures must be used to correct for the aberrations introduced by an optically thick source [17, 24]. Other problems can include aliasing of data and the inability of the reconstruction algorithms to faithfully reproduce discontinuous structures in the object. Despite these limitations, computed tomography can provide information about an object which would be difficult or impossible to obtain by other means. In the second part of this series of papers, the construction and utilization of an instrument for collecting and processing CT emission data from common spectroscopic sources will be described. Practical examples of the utility of tomographic image reconstruction will be presented.

ACKNOWLEDGMENTS

The authors would like to thank G. T. HERMAN for providing the SNARK77 image-reconstruction program. The generous support of the National Science Foundation (grant numbers CHE-83-20053, CHE-83-09446, and CHE-84-05851) American Cyanamid, and SOHIO is also acknowledged.

LITERATURE CITED

1. Scheeline, A.; Walters, J. P. "Spatially Resolved Spectroscopy: Theory and Applications of the Abel Inversion" in: *Contemporary Topics in Analytical and Clinical Chemistry*, Vol. 4; Eds. D. M. Hercules, G. M. Hieftje, L. R. Snyder, and M. A. Evenson, Plenum Press, New York (1982).
2. R. N. Bracewell, *Aust. J. Phys.* **9**, 198 (1956).
3. O. H. Nester and H. H. Olsen, *SIAM Rev.* **2**, 200 (1960).
4. C. J. Cremers and R. C. Birkebak, *Appl. Opt.* **5**, 1057 (1966).
5. B. S. Choi and H. Kim, *Appl. Spectrosc.* **36**, 71 (1982).
6. J. D. Algeo and M. B. Denton, *Appl. Spectrosc.* **35**, 35 (1981).
7. M. M. Prost, *Spectrochim. Acta* **37B**, 541 (1982).
8. M. W. Blades and G. Horlick, *Appl. Spectrosc.* **34**, 696 (1980).
9. Y. Yasutomo, K. Miyata, S. Himenomo, T. Enoto and Y. Ozawa, *IEEE Trans. on Plasma Sci.* **PS-9**, 18 (1981).
10. M. W. Blades, *Appl. Spectrosc.* **37**, 371 (1983).
11. J. Radon, *Berichte Sachsische Akademie der Wissenschaften, Leipzig, Mathematisch - Physikalische Klasse* **69**, 262 (1917).
12. S. R. Deans, "The Radon Transform" in: *Mathematical Analysis of Physical Systems*, Ed. R. E. Mickens, Van Nostrand, New York (1985).
13. G. T. Herman, *Image Reconstruction from Projections: The Fundamentals of Computerized Tomography*, Academic Press, New York (1980).
14. S. W. Rowland, "Computer Implementation of Image Reconstruction Formulas" in *Image Reconstruction from Projections: Implementation and Applications*, Ed. G. T. Herman, Springer-Verlag, New York (1979).
15. R. Gordon, "Three-Dimensional Reconstructions from Projections: A Review of Algorithms" in *International Review of Cytology*, Vol. 38, Eds. G. H. Bourne and J. F. Danielli, Academic Press, New York (1974).
16. W. Hendee, *The Physical Principles of Computed Tomography*; Little, Brown and Co., Boston (1983).
17. T. G. Budinger, G. T. Gullberg and R. H. Huesman, "Emission Computed Tomography" in *Image Reconstruction from Projections: Implementation and Applications*, Ed. G. T. Herman, Springer-Verlag, New York (1979).

18. G. N. Ramachandran and A. V. Lakshminarayanan, *Proc. Nat. Acad. Sci. USA* 68, 2236 (1971).
19. R. M. Mersereau, *Comp. Biol. Med.* 68, 247 (1976).
20. R. A. Crowther, D. J. DeRosier and A. Klug, *Proc. Roy. Soc. Lond. A* 317, 319 (1970).
21. Wayne G. Roberge, private communication, August (1987).
22. A. Klug and R. A. Crowther, *Nature* 238, 435 (1972).
23. R. W. Ramirez, *The FFT: Fundamentals and Concepts* Prentice-Hall, Englewood, New Jersey (1985).
24. M. K. Salakhov, E. V. Sarandayev and I. S. Fishman, *Comp. Enhan. Spectrosc.* 1, 213 (1983).

Figure Captions

Figure 1 Illustration of the method of backprojection for a homogeneous, square object in the X-Y plane.

Figure 2 Illustration of the convolution of a lateral projection, A. Lateral profile of Ca I emission from an ICP. This profile is the least-square regression polynomial [5] to Ca I emission at 1 mm below the tip of the initial radiation zone in a 1.25 kW plasma., B. PARZN convolution filter [17] in the frequency domain, C. Convolved lateral projection.

Figure 3 An illustration of image reconstruction by Fourier inversion. DFT refers to a discrete Fourier transform, and 2DIFT to a two dimensional inverse Fourier transform.

Figure 4 Example of the process of iterative image reconstruction. See text for discussion.

Figure 5 Reconstruction of an object by different CT algorithms. A. Phantom; B. Fourier path; C. rho-filtered layergram; D. filtered backprojection (convolution).

Figure 6 The effect of reducing the number of angles (over a total of 180°) at which lateral projections are collected. A. Phantom; B. Five equally spaced angles; C. 25 equally spaced angles; D. 125 equally spaced angles. Convolution algorithm, 99 lateral detector positions.

Figure 7 The effect of reducing the number of detector positions or elements in each angular lateral projection. A. Phantom; B. 11 detector positions; C. 33 detector positions; D. 99 detector positions. Convolution algorithm, 125 viewing angles.

Figure 8 The effect of noise in the lateral-projection data on the quality of the reconstructed image. A. Phantom; B. no noise; C. $S/N = 10$; D. $S/N = 2$; E. $S/N = 1$; F. $S/N = 0.1$. Convolution algorithm, 99 lateral positions, 125 viewing angles.

Figure 9 Comparison of inverse Abel transformation and CT for image reconstruction of a circularly symmetric object. A. Phantom; B. Phantom contour plot; C. Image reconstructed by CT using a convolution algorithm with 60 viewing angles and 101 lateral positions; D. Contour plot of image reconstructed by CT; E. Image reconstructed by inverse Abel transformation from a projection at 0 degrees; F. Image reconstructed by inverse Abel transformation from a projection at 90 degrees.

Figure 10 Comparison of inverse Abel transformation and CT for image reconstruction of an elliptically symmetric object. A. Phantom; B. Phantom contour plot; C. Image reconstructed by CT (same conditions as in Figure 9.); D. Contour plot of image reconstructed by CT; E. Image reconstructed by inverse Abel transformation from a projection at 0 degrees; F. Image reconstructed by inverse Abel transformation from a projection at 90 degrees.

Figure 11 Comparison of inverse Abel transformation and CT for image reconstruction of a elliptically skewed object. A. Phantom; B. Phantom contour plot; C. Image reconstructed by CT (same conditions as in Figure 9.); D. Contour plot of image reconstructed by CT; E. Image reconstructed by inverse Abel transformation from a projection at 0 degrees; F. Image reconstructed by inverse Abel transformation from a projection at 90 degrees.

Figure 12 Comparison of inverse Abel transformation and CT for image reconstruction of an elliptically skewed object with an off-axis hole. A. Phantom; B. Phantom contour plot; C. Image reconstructed by CT (same conditions as in Figure 9.); D. Contour plot of image reconstructed by CT; E. Image reconstructed by inverse Abel transformation from a projection at 0 degrees; F. Image reconstructed by inverse Abel transformation from a projection at 90 degrees.

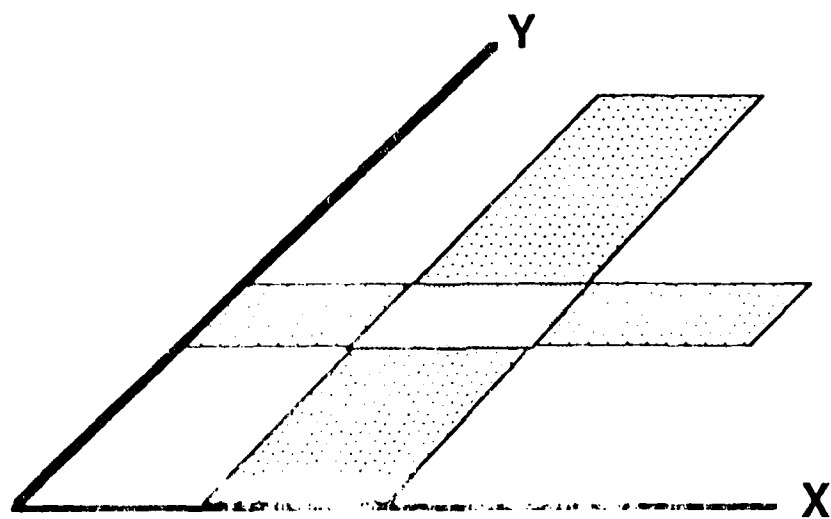
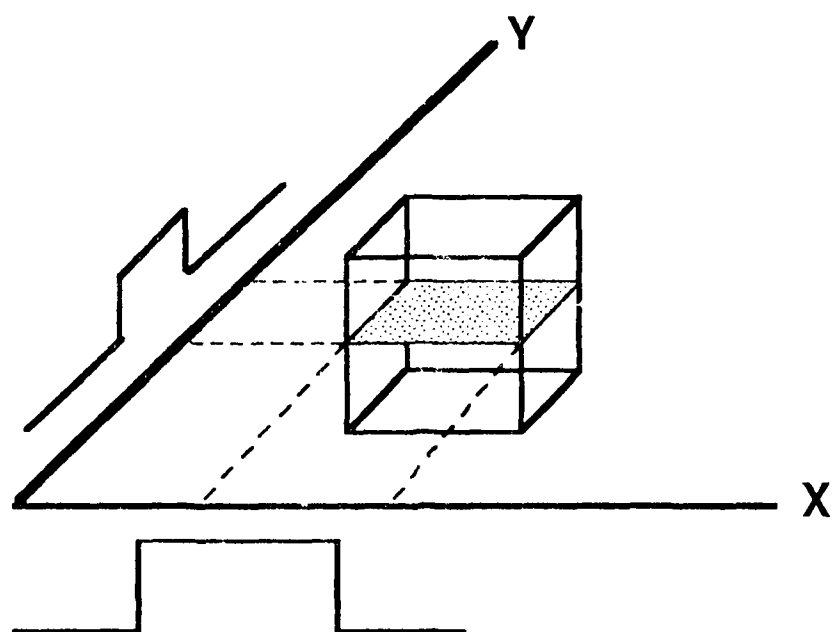
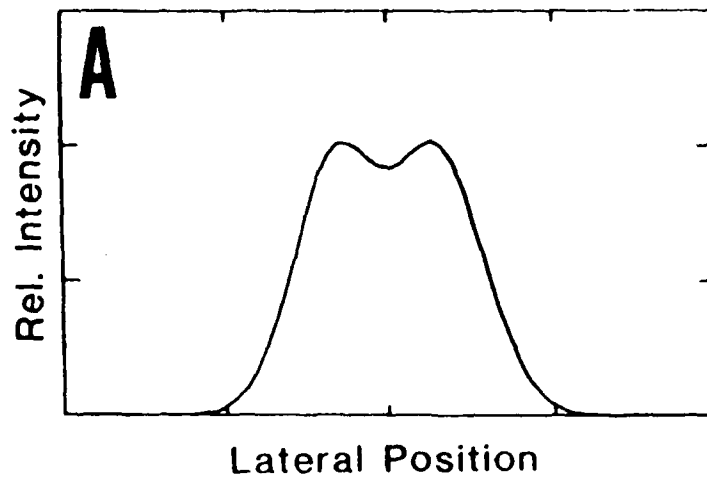
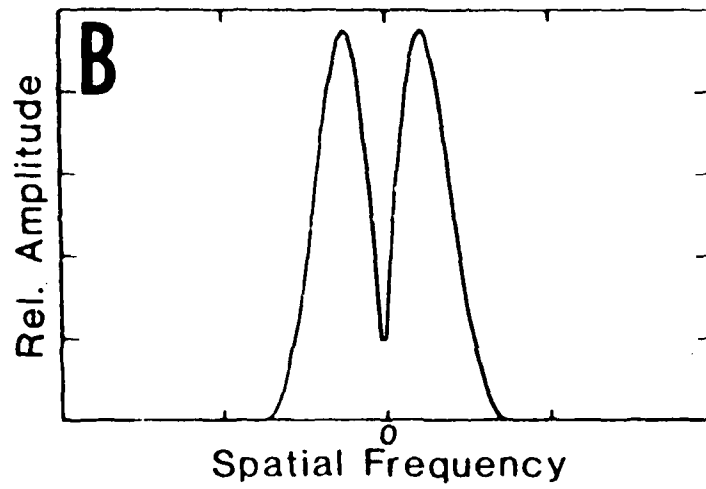


Fig 1

Lateral Profile



Filter Function



Filtered Projection

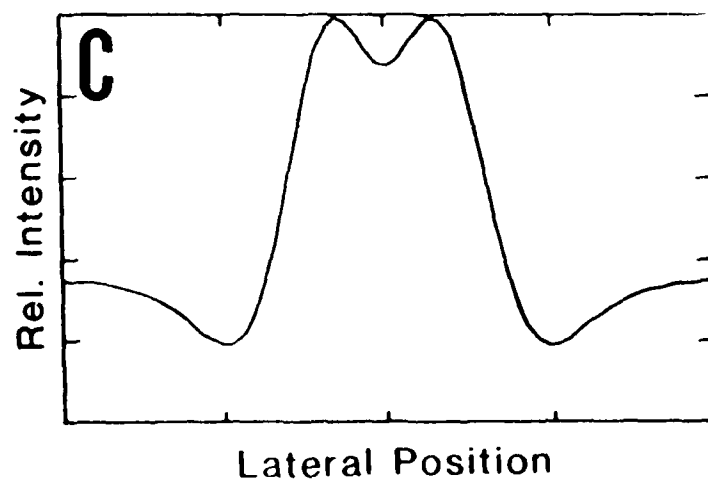


Fig. 2

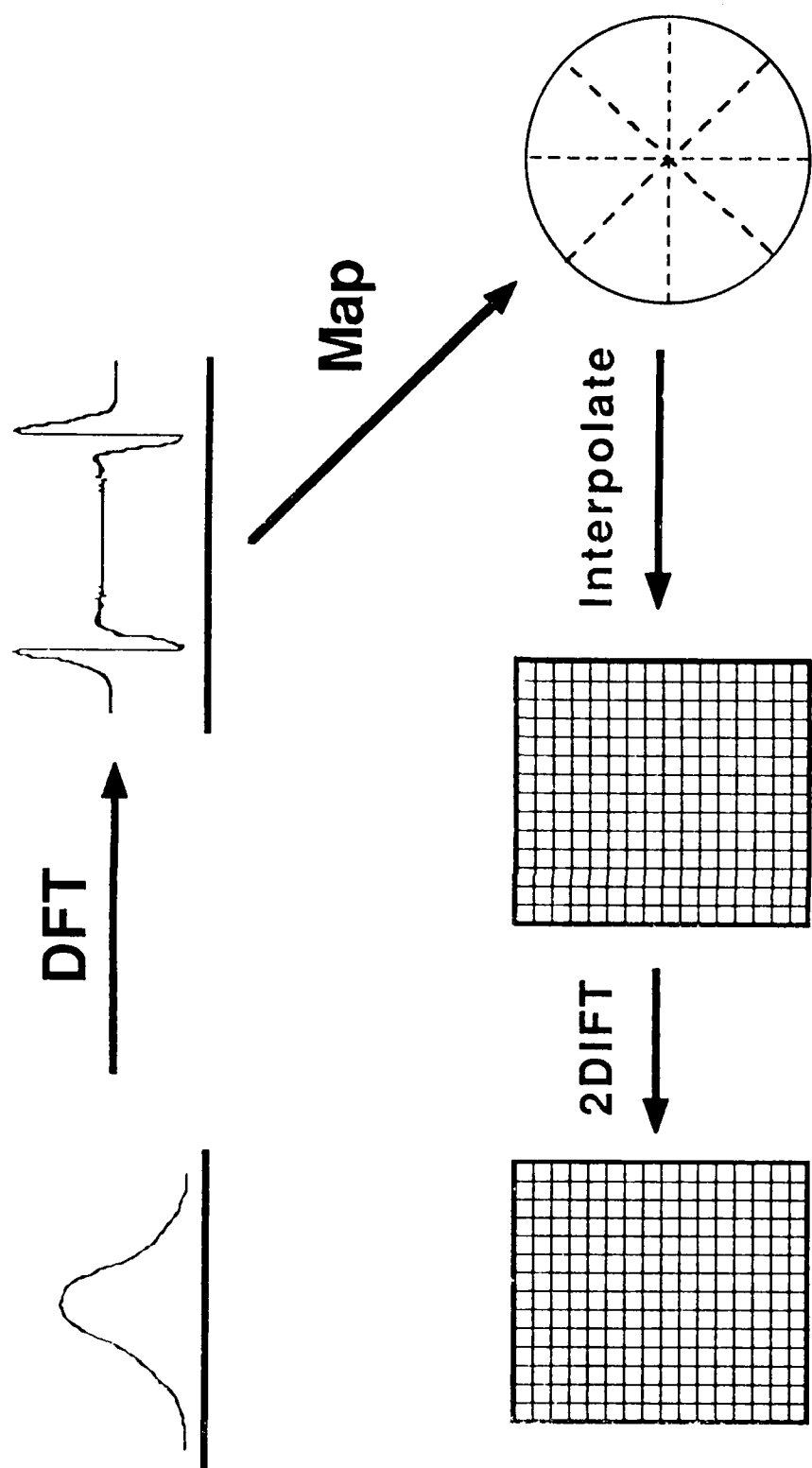


Fig. 3

1	2	5	→ 8
4	3	1	→ 8
2	5	4	→ 11

2 (1.4)	3 (2.2)	6 (4.4)	→ 11
4 (3.2)	4 (3.2)	2 (1.6)	→ 10
1 (1)	4 (4)	6 (6)	→ 11

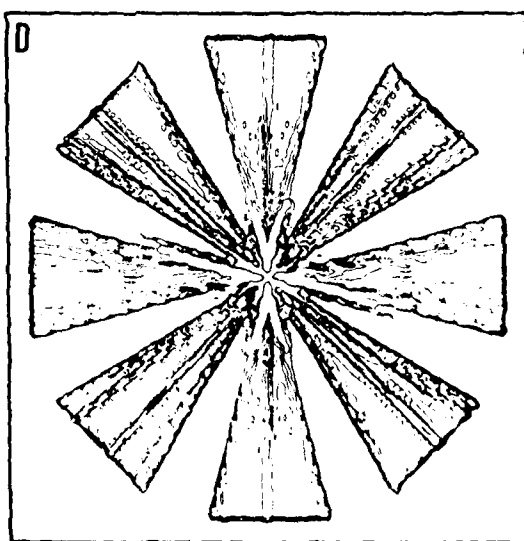
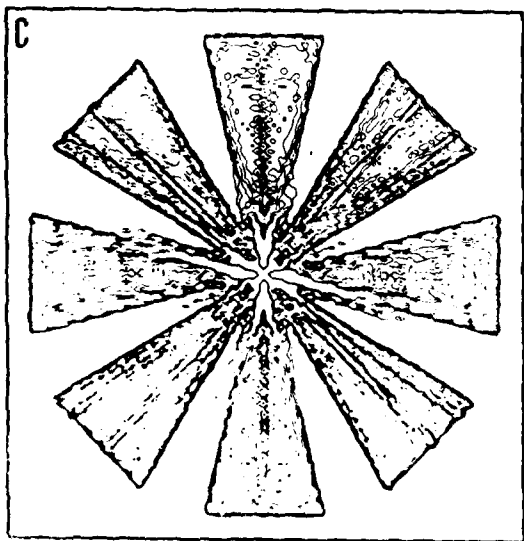
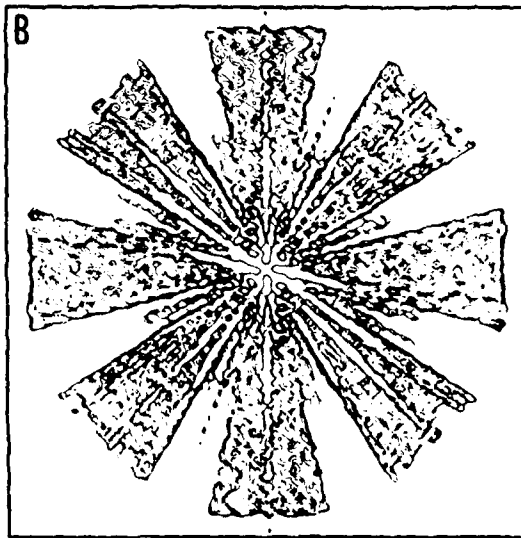
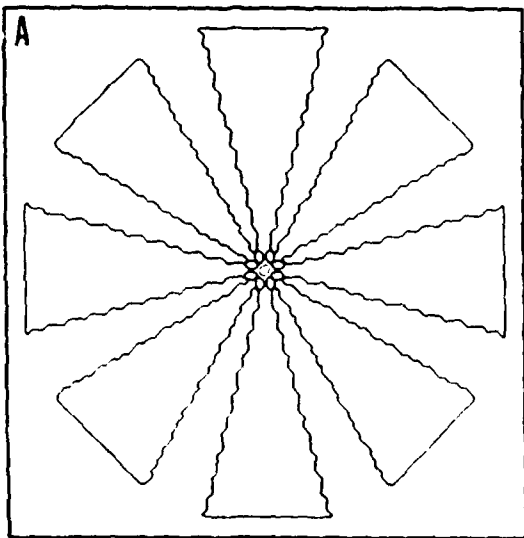
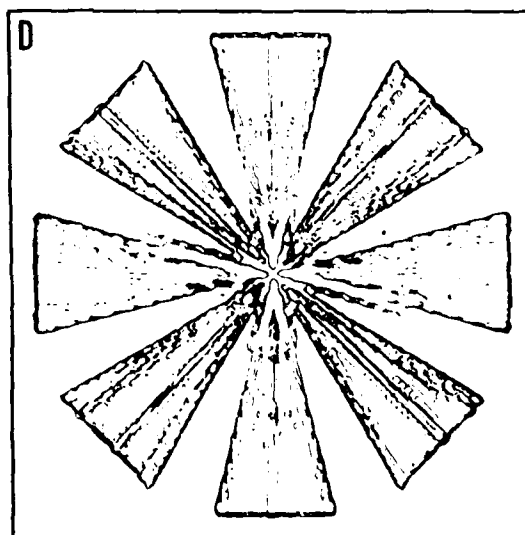
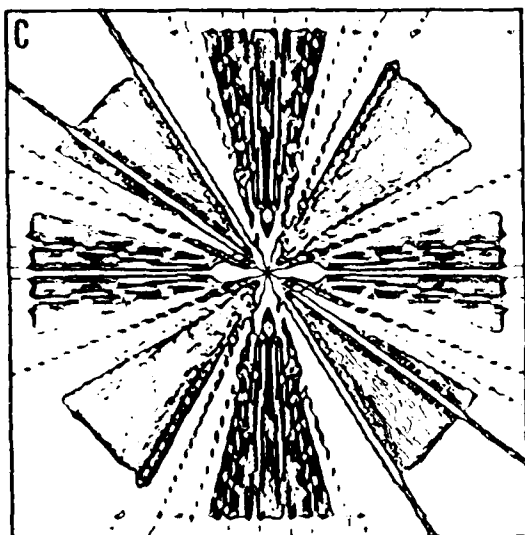
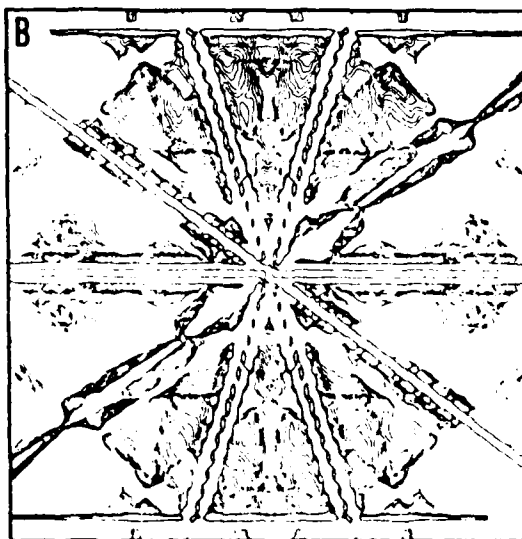
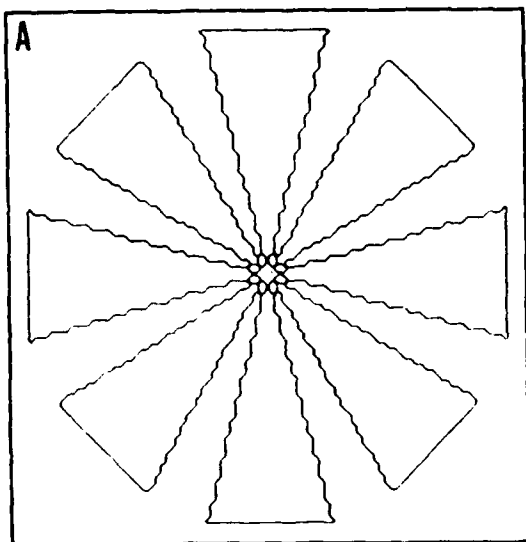


Fig. 5



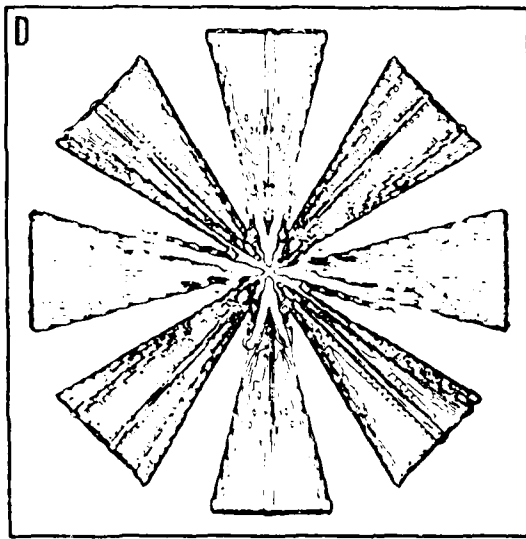
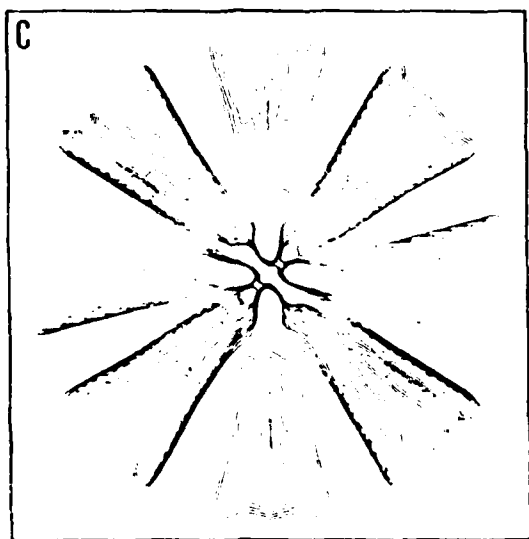
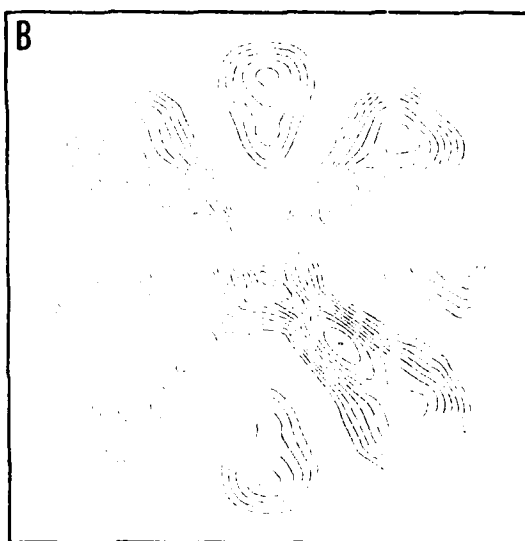
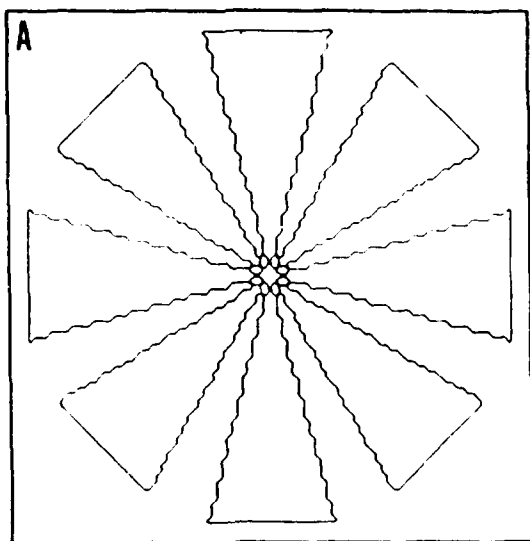


Fig 7

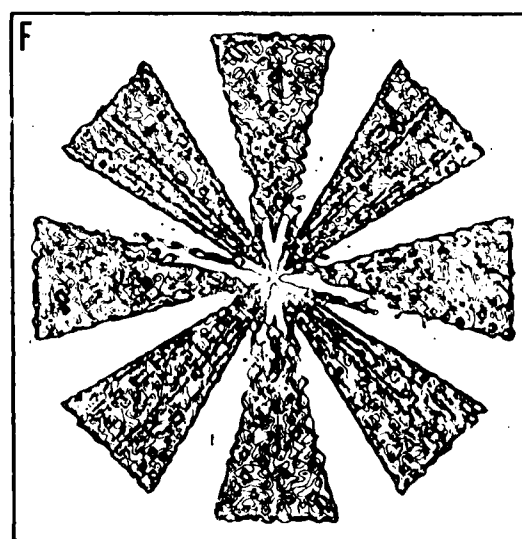
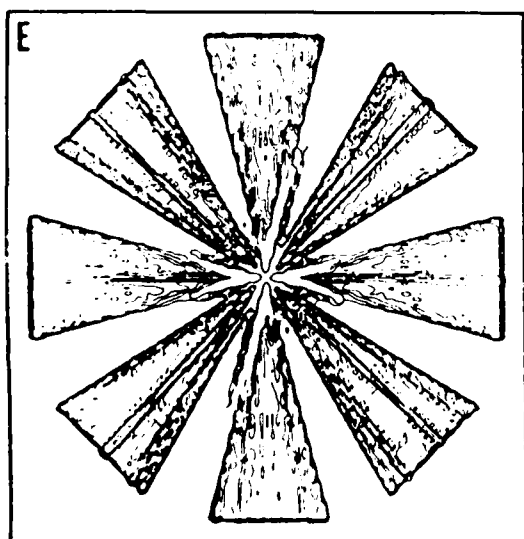
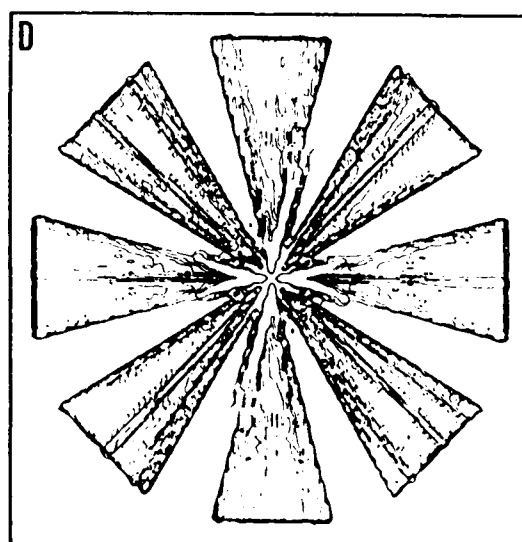
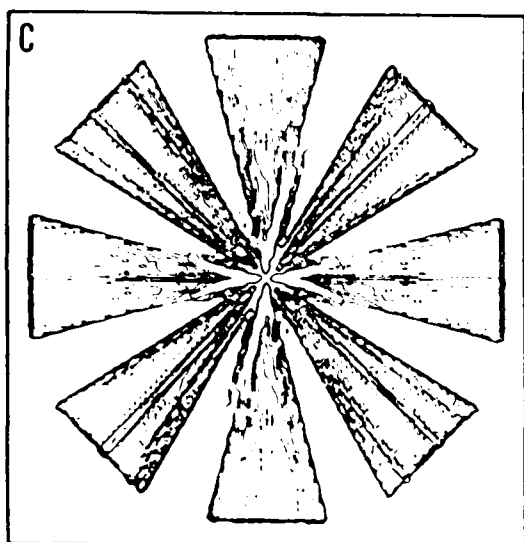
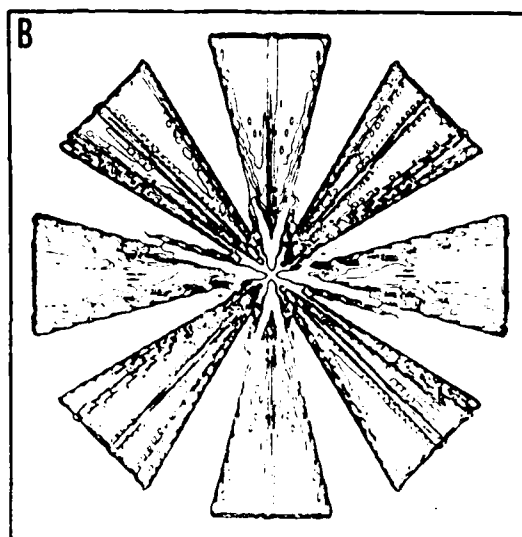
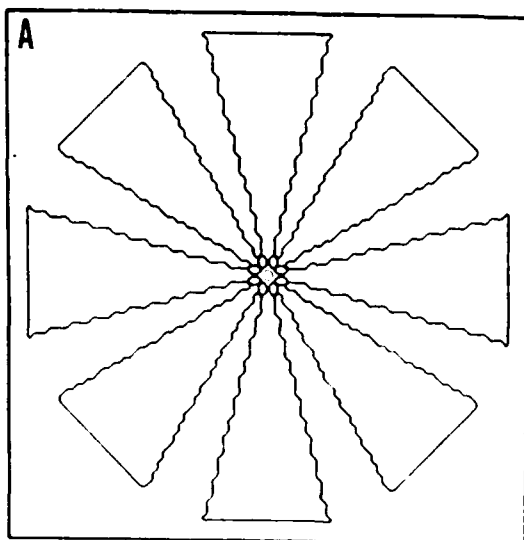


Fig. 8

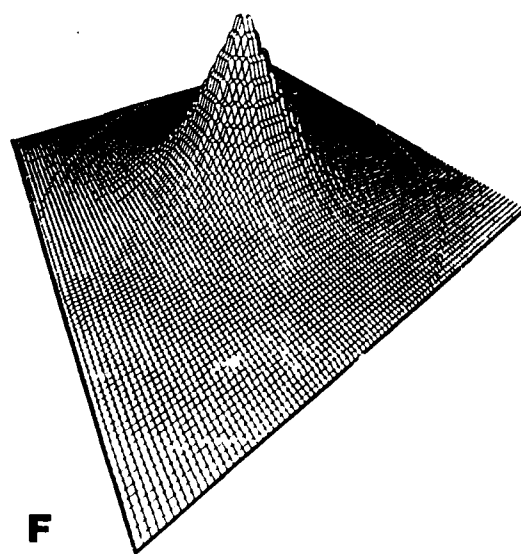
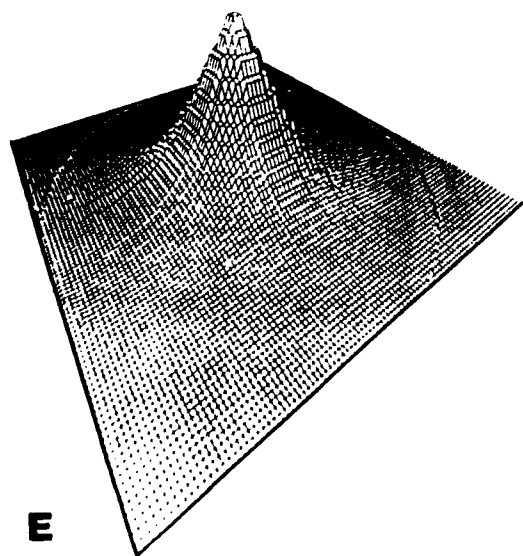
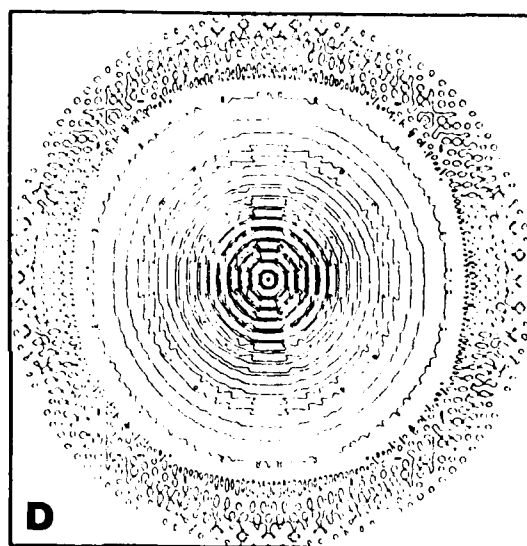
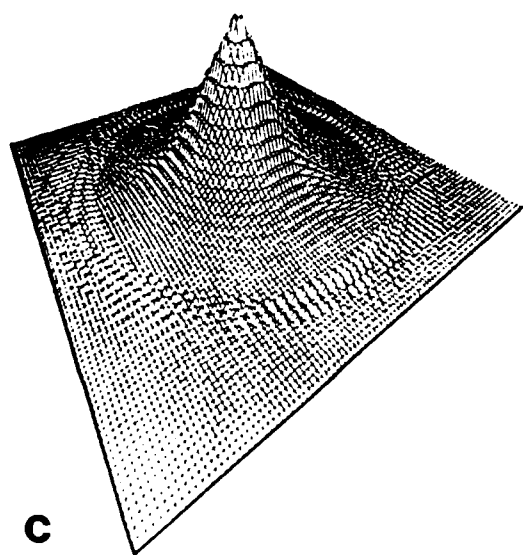
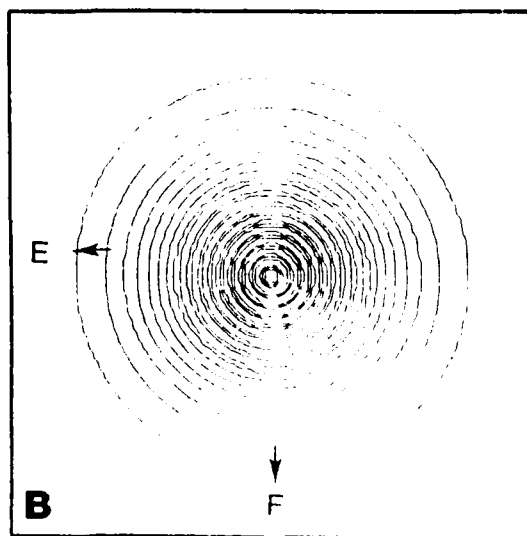
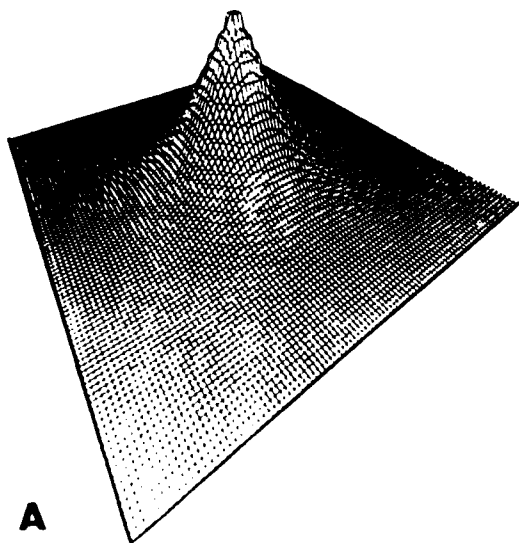


Fig 9

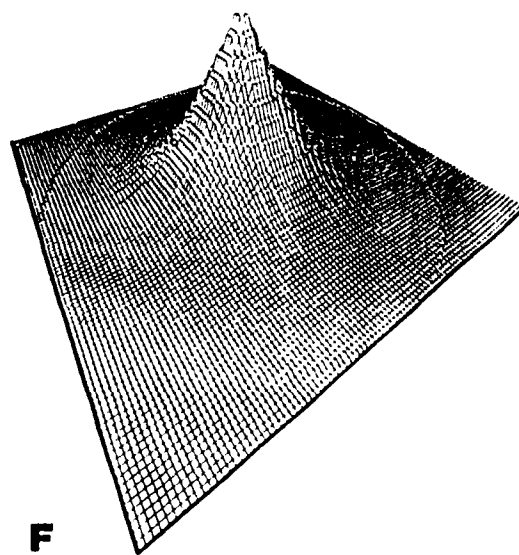
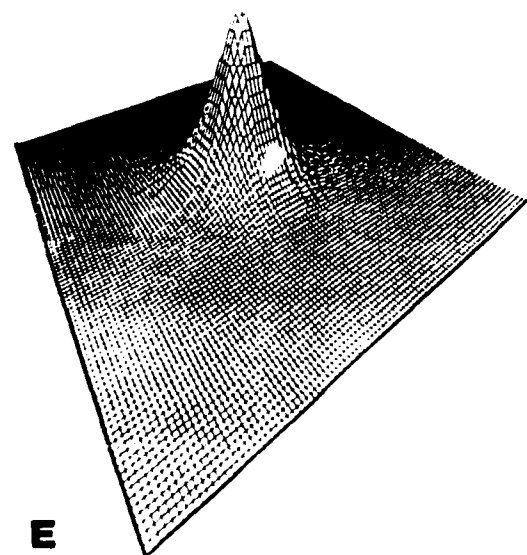
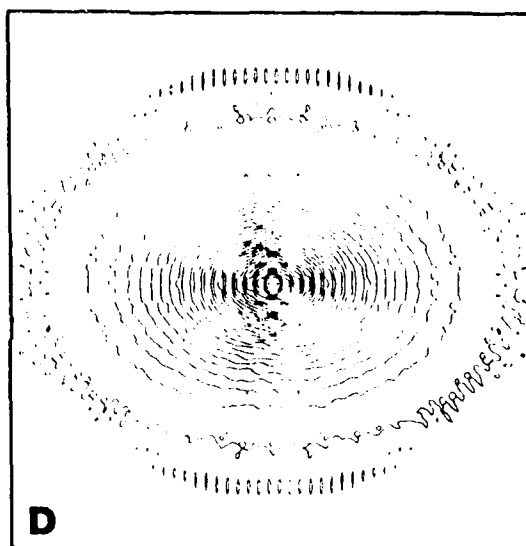
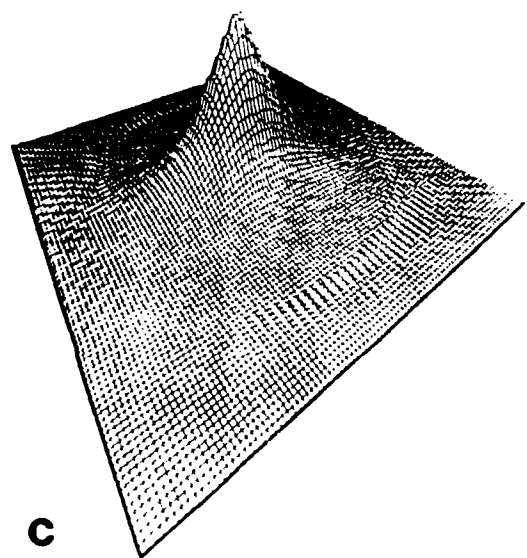
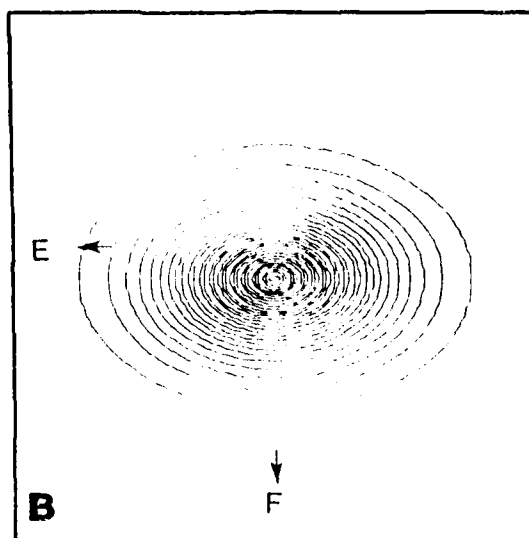
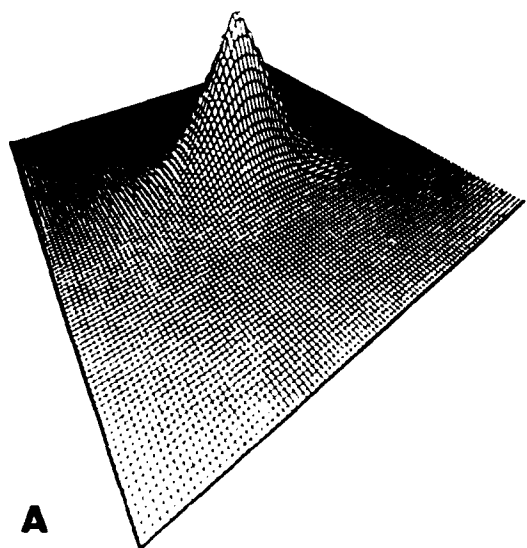


Fig. 10

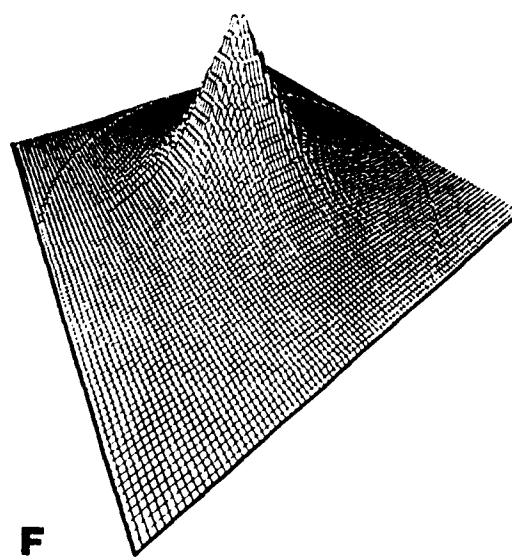
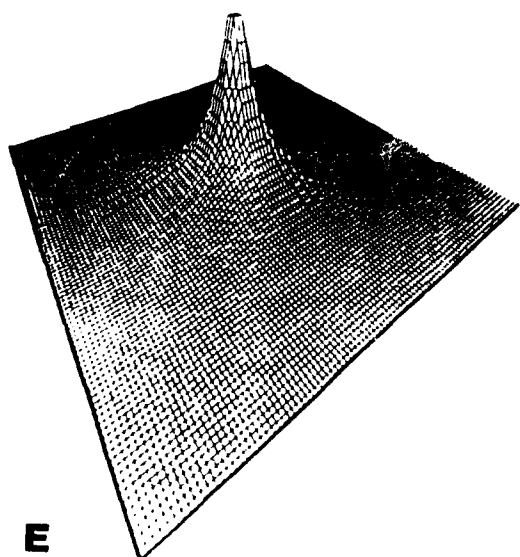
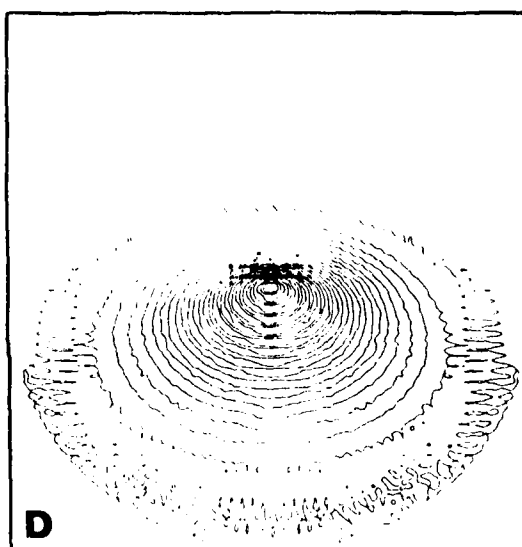
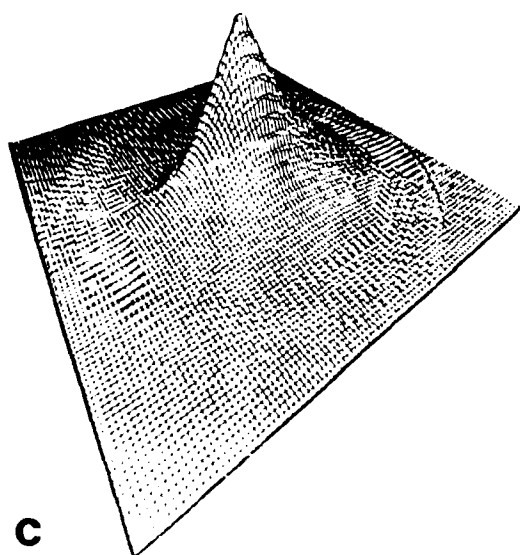
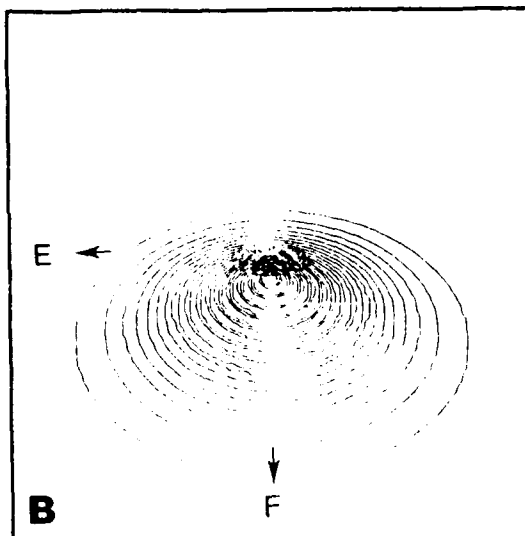
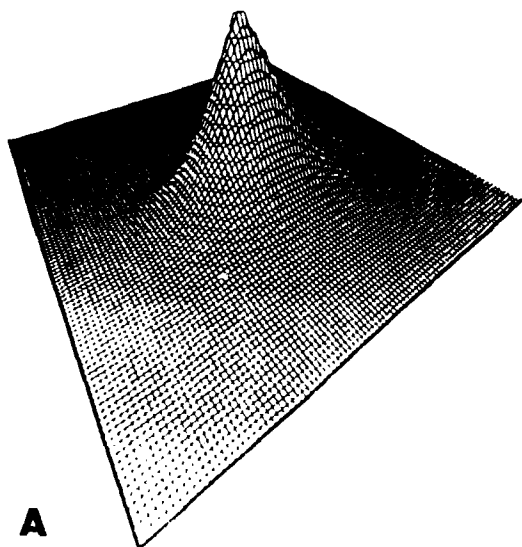


Fig. 11

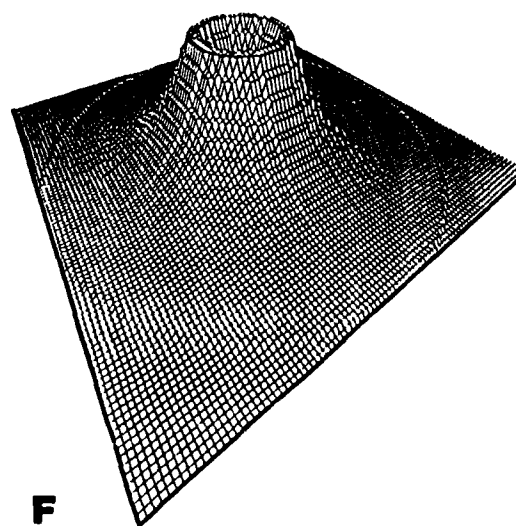
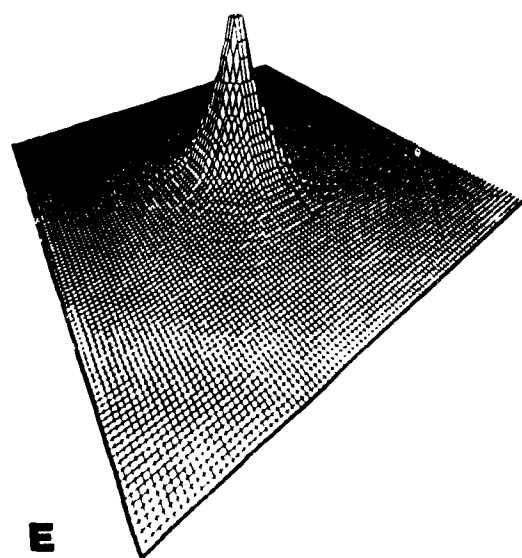
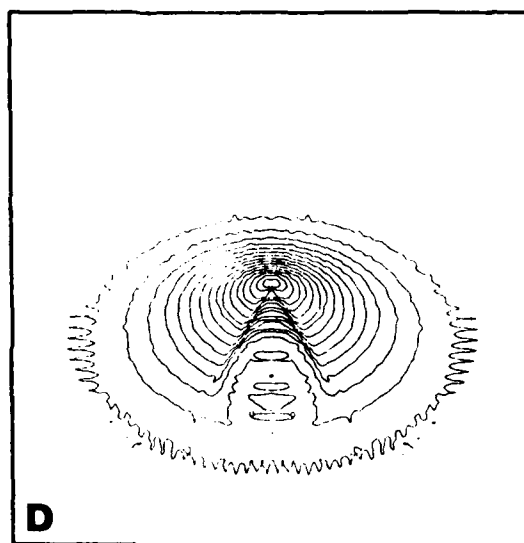
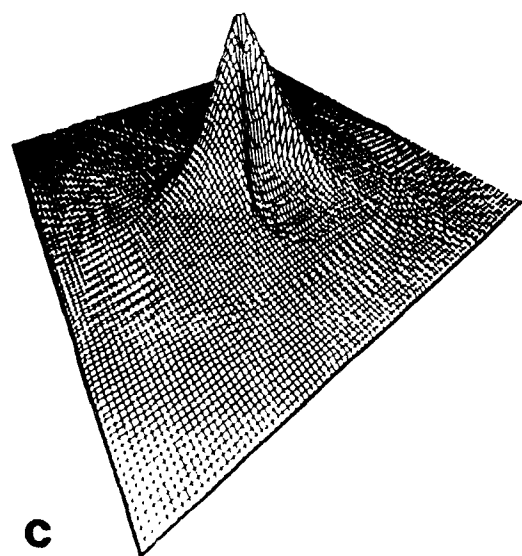
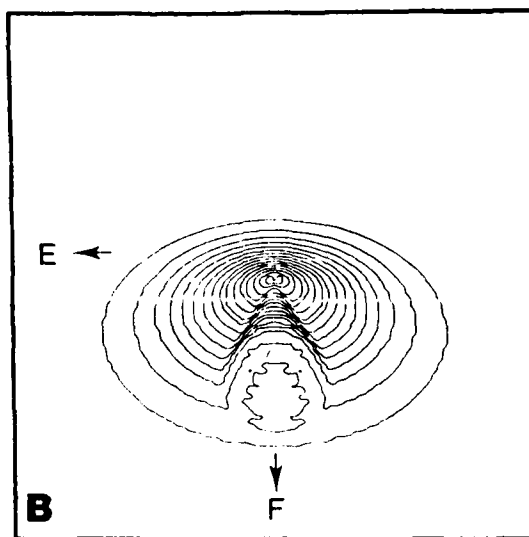
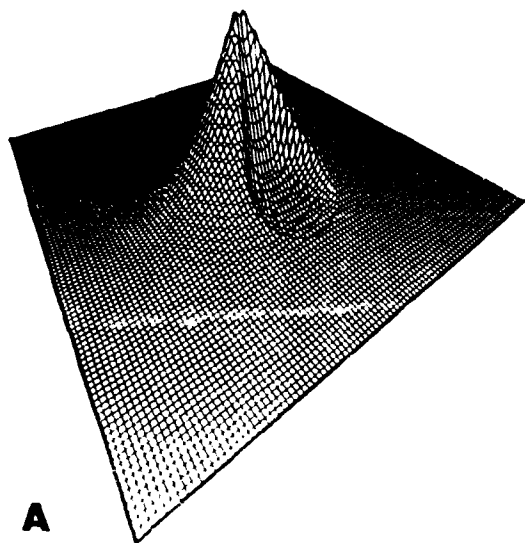


Fig. 12

TECHNICAL REPORT DISTRIBUTION LIST, GEN

	<u>No. Copies</u>		<u>No. Copies</u>
Office of Naval Research Attn: Code 1113 800 N. Quincy Street Arlington, Virginia 22217-5000	2	Dr. David Young Code 334 NORDA NSTL, Mississippi 39529	1
Dr. Bernard Douda Naval Weapons Support Center Code 50C Crane, Indiana 47522-5050	1	Naval Weapons Center Attn: Dr. Ron Atkins Chemistry Division China Lake, California 93555	1
Naval Civil Engineering Laboratory Attn: Dr. R. W. Drisko, Code L52 Port Hueneme, California 93401	1	Scientific Advisor Commandant of the Marine Corps Code RD-1 Washington, D.C. 20380	1
Defense Technical Information Center Building 5, Cameron Station Alexandria, Virginia 22314	12 high quality	U.S. Army Research Office Attn: CRD-AA-IP P.O. Box 12211 Research Triangle Park, NC 27709	1
DTNSRDC Attn: Dr. H. Singerman Applied Chemistry Division Annapolis, Maryland 21401	1	Mr. John Boyle Materials Branch Naval Ship Engineering Center Philadelphia, Pennsylvania 19112	1
Dr. William Tolles Superintendent Chemistry Division, Code 6100 Naval Research Laboratory Washington, D.C. 20375-5000	1	Naval Ocean Systems Center Attn: Dr. S. Yamamoto Marine Sciences Division San Diego, California 92132	1